

Review

The Recent Progress of Two-Dimensional Transition Metal Dichalcogenides and Their Phase Transition

Hui Chen ¹, Jiwei Zhang ¹, Dongxiao Kan ², Jiabei He ², Mengshan Song ², Jianhua Pang ^{1,*}, Songrui Wei ^{3,*} and Kaiyun Chen ^{2,*}

¹ School of Mechanical Engineering, Guangdong Ocean University, Zhanjiang 524088, China

² Advanced Materials Research Central, Northwest Institute for Nonferrous Metal Research, Xi'an 710016, China

³ Institute of Microscale Optoelectronics, Shenzhen University, Shenzhen 518060, China

* Correspondence: njpjh@sina.com (J.P.); weisongrui@126.com (S.W.); chenkaiyun309@gmail.com (K.C.)

Abstract: Graphene is attracting much attention in condensed matter physics and material science in the two-dimensional(2D) system due to its special structure, and mechanical and electronic properties. However, the lack of electronic bandgap and uncontrollable phase structure greatly limit its application in semiconductors, such as power conversion devices, optoelectronic devices, transistors, etc. During the past few decades, 2D transition metal dichalcogenides (TMDs) with much more phase structures have attracted intensive research interest in fundamental studies and practical applications for energy storage, as catalysts, and in piezoelectricity, energy harvesting, electronics, optoelectronic, and spintronics. The controllable phase transition also provides another degree of freedom to pave the way for more novel devices. In this review, we introduce the abundant phase structures of 2D-TMDs, including 2H, 1T, 1T' and charge density waves, and highlight the corresponding attractive properties and applications of each phase. In addition, all the possible methods to trigger the phase transition in TMDs are systematically introduced, including strain engineering, electron doping, alloying, thermal, electric field, and chemical absorption. Finally, the outlook of future opportunities in TMD phase transitions and the corresponding challenges, including both the synthesis and applications, are also addressed.

Keywords: transition metal dichalcogenides; charge density waves; ferromagnetism; photodetector; phase transition



Citation: Chen, H.; Zhang, J.; Kan, D.; He, J.; Song, M.; Pang, J.; Wei, S.; Chen, K. The Recent Progress of Two-Dimensional Transition Metal Dichalcogenides and Their Phase Transition. *Crystals* **2022**, *12*, 1381. <https://doi.org/10.3390/cryst12101381>

Academic Editor: Shouxun Ji

Received: 25 August 2022

Accepted: 24 September 2022

Published: 28 September 2022

Publisher's Note: MDPI stays neutral with regard to jurisdictional claims in published maps and institutional affiliations.



Copyright: © 2022 by the authors. Licensee MDPI, Basel, Switzerland. This article is an open access article distributed under the terms and conditions of the Creative Commons Attribution (CC BY) license (<https://creativecommons.org/licenses/by/4.0/>).

1. Introduction

Graphene, as a typical 2D material, did not widely concern researchers because many theoretical calculations suggested the instability of the monolayer structure. In 2004, physicists from the University of Manchester, A. K. Geim and K. S. Novoselov, successfully separated the stable monolayer graphene through micromechanical exfoliation for the first time, leading to rising in graphene [1]. The special bonding mechanism between carbon atoms also provides graphene with toughness [2,3]. In terms of electronic structure, graphene is semi-metal and has ultra-high conductivity, which is much higher than traditional precious metal conductive materials, such as gold, silver, and copper. As a 2D material, graphene has a 2D honeycomb-like structure formed by sp^2 -hybridization between six carbon atoms in a plane and has a large specific surface area, and, therefore, it is widely used as electrode material for lithium-ion batteries and supercapacitors [4]. In addition, graphene also shows excellent performance in electronic, optical, and energy storage devices, FET, sensors, nanogenerators, biomedicine, and many other fields [5–7]. However, graphene's zero band gap greatly limits its further applications [8]. Therefore, the search for a 2D material similar to graphene and able to avoid the shortcomings of graphene has become an urgent matter in physical, chemical, material, and device research.

In recent years transition metal dichalcogenide (TMD) has become a much more attractive novel 2D material due to its unique physical and chemical properties, leading to

broad application prospects in many fields such as nanoelectronics or optical devices [9–12], logic gate [13–15], organic light-emitting diode (OLED) pixel driver [16,17], memory [18] and so on. At present, more than 40 kinds of 2D TMDs have been discovered. The chemical formula of TMDs can be expressed as MX_2 (M represents the transition metal elements of group IV B ~ X B, X represents S, Se, and Te). TMDs containing group IV B ~ VII B transition metal elements have layered structures, while TMDs containing group VIII B ~ X B transition metal elements have a non-layered structure [19]. According to its band structure, the conductivity range of bulk TMDs includes HfS_2 insulators, semiconductors, such as MoS_2 and WS_2 , and real metals, such as NbS_2 and VSe_2 [20]. Due to the van der Waals interaction between the interlayers, 2D TMD exhibits unique stratified chemistry. Any change in the nano-layered structure has a quantum size effect on its physical and chemical properties [21]. Unlike graphene, TMDs are more abundant in composition and crystal structure, including 2H, 1T, 1T', and have various charge density waves (CDWs).

Many physical and chemical properties of TMDs are closely related to their phases. Therefore, the study of phase-related characteristics is of great significance to promote the basic research of TMDs. Unlike graphene, the properties of TMDs vary with their phases, for example, 2H- MoS_2 is semi-conductive, 1T- MoS_2 is metallic, and 1T'- MoS_2 is semi-metallic [22–24]. The band structures of 2H- MoS_2 , 1T- MoS_2 and 1T'- MoS_2 are shown in Figure 1. The diverse nature of TMDs means they are destined to be widely used in many fields. Due to their excellent catalytic [25], optical [26], electronic [27], magnetic [28] and ultra-high carrier performance [29], TMDs have been widely studied as catalysts in the hydrogen evolution reaction (HER) [30], in potassium ion batteries [31], as supercapacitors [32], for photoelectric devices [33], for magnetic devices [34] and for other applications. In addition, superconductivity and strongly correlated electron system phenomena appear in the CDW phase [35]. TMDs exhibit a number of properties related to their phases. In order to explore the application of TMDs materials, it is necessary to study their related properties.

Several recent reviews have covered the physical properties, potential applications, and phase engineering of TMDs [23,36–40]. In this review, we comprehensively and emphatically introduce the characteristics of TMDs and their related phase applications and phase transformation engineering, and we outline the abundant phases of 2D TMDs. At the same time, the attractive properties of TMD phases and their applications are introduced. In addition, the possible methods of triggering TMD phase transition, including strain engineering and electric field regulation, are summarized in detail. Finally, we look forward to the future opportunities and corresponding challenges of TMD phase transition.

2. The Atomic Crystal Structure of TMDs

2.1. 2H, 1T, and 1T' Phase Structures

The variety of atom types and distribution within the material results in TMDs having more abundant crystal structures compared to that of graphene. The sandwich structure of 2D-TMDs consists of a middle layer, composed of transition metal atoms, and two sides, composed of S group atoms. Therefore, the different structures of 2D TMDs depend on the stacking modes of three-layer atoms. The two most common structures in TMDs are the trigonal prismatic 2H phase and the octahedral 1T phase (Figure 1). The 2H phase can be viewed as A-B-A stacking, in which the chalcogens located in different layers occupy the same site (in-plane site alignment) with mirror symmetry to the metal atom surface. Differing from 2H, the 1T phase can be seen as a structure composed of an ABC stacking manner and being centrosymmetric. Besides the 2H and 1T phases, another common structure is the 1T' phase. This structure can be regarded as the periodic distorted 1T phase with two neighboring metals close to each other and forming a metal zig-zag chain. The metal–metal chemical bond is a “dimer bond” [41]. The 1T' is often observed in group V B TMDs. The stabilities of the 2H, 1T, and 1T' phases are very different depending on the combinations of transition metal elements (IV B to X B) and chalcogens (S, Se, and Te). At present, the known 2H and 1T phase TMD materials are mainly the dihalides of Nb,

Mo, Ta, and W. Thermodynamic stable phase structure is always associated with the 2H or 1T phases, while other structures are always metastable phases. For example, among the TMDs of group VI B, there are six combinations of TMDs, of which five (except WTe_2) are the 2H phase as the most stable phase and the 1T phase as the metastable phase.

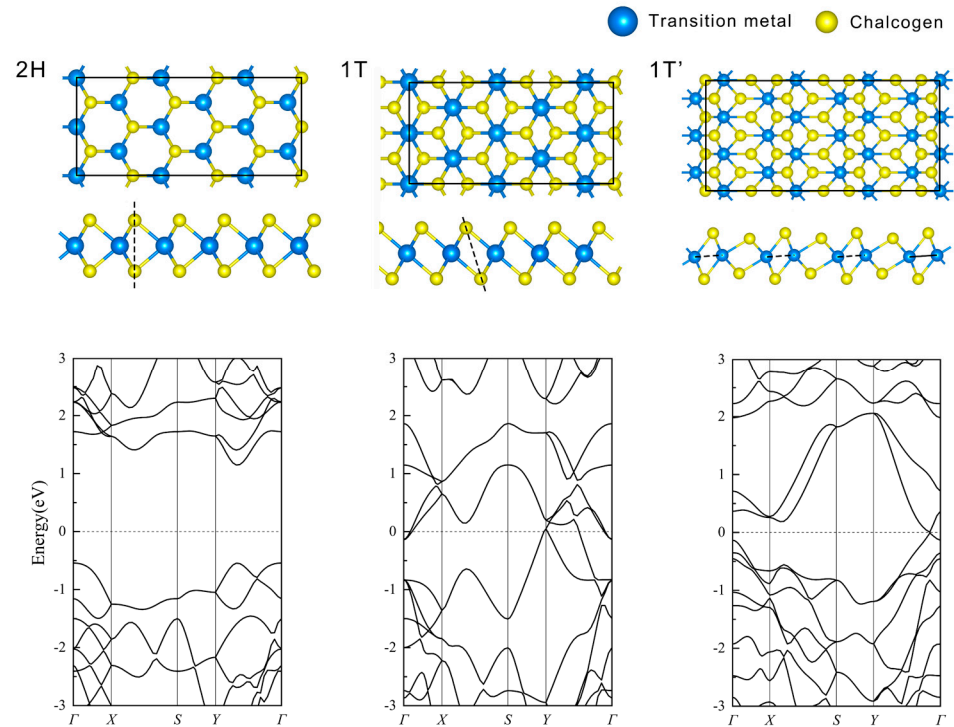


Figure 1. Monolayer atomic structure and band structure of TMDs in 2H, 1T, and 1T' phases.

2.2. Charge Density Waves

In addition to the above three structures, a series of more complex structures have also been observed in TMDs. The characteristics of these structures are that the crystal structure is distorted, based on 2H and 1T, which leads to a certain degree of modulation distribution of the charge density in TMDs, showing the characteristics of the periodic change of the charge density with the lattice [42–44]. Figure 2 shows the phase transition in multiple physical domains [45]. It can be seen that the CDW of the material varies under different temperature and pressure conditions. CDW was first discovered in the periodic distortion of one-dimensional metal chains at low temperatures. The main physical mechanism for its generation is coupling between electrons and phonons. When electrons in the same quantum state repel each other and open a certain band gap at the Fermi surface (metal–insulation transition), the crystal structure changes. Periodic distortion occurs, which leads to modulation of the spatial distribution of charge density within the material system [46]. Chan and Heines proved that CDWs do not appear in systems where electrons and phonons are not coupled [47].

The CDWs of TMDs have received extensive attention, mainly because of their unconventional superconducting phenomena and strongly correlated electronic systems [48]. In addition, due to the diversity of CDWs, some new phenomena and peculiar properties can be achieved by modulating CDWs, such as the implementation of superconductivity under chemical doping, and the catalytic performance of surfaces controlled by the absorptivity of reactants and active sites in CDWs [49–52]. Quasi-one-dimensional Sn metal atomic chains can be grown on the surface of superlattice NbTe_2 modulated by CDWs, and the transition between metalloid and metallicity induces the electronic properties of the surface [53]. This provides a great possibility for using CDWs to control the surface properties of materials for special hetero catalysis, epitaxial growth of low-dimensional materials, and other nano-electronic devices.

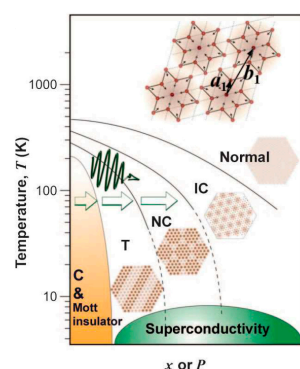


Figure 2. Phase and electronic structures of TMDs. General phase diagram of 1T-TaS₂ in different physical domains (temperature, doping $x(\text{Fe})$, or pressure P). Where C refers to commensurate CDW, T refers to triclinic incommensurate CDW, NC refers to near commensurate and IC refers to incommensurate CDW. The phase evolution of a CDW can be characterized by the variation of the hexagonal CDW diffraction peak at the inverse vector Q (upper right corner). The upper right corner shows the SD 13-cluster, representing the C-CDW cells in real space. Lattice distortion within each star is coupled with strong charge density redistribution. Reproduced from [45], with the permission of the AAAS.

3. Performance and Application of 2D TMDs

Some bulk TMDs are similar to graphene and layered materials with van der Waals interaction between two neighboring layers. Due to the weak van der Waals interaction, 2D TMDs can be obtained using a stripping method similar to graphene. In addition, chemical vapor deposition (CVD) can also be used to prepare 2D TMDs [54]. The emergence of 2D TMDs has greatly enriched catalysis applications, energy storage, ferrous materials, electronics, and spintronics.

3.1. Catalyst of Hydrogen Evolution Reaction

As bulk TMD is reduced to a monolayer, van der Waals interactions are no longer present at the surface, while chalcogen atoms and transition metal atoms are exposed at the surface. Therefore, the surface of 2D TMDs often show high chemical activity serving as a catalyst in HER. Experimental studies reported that monolayer MoS₂ has excellent catalysis [55,56]. However, the excellent catalytic performance of 2H-MoS₂ should mainly be attributed to the high chemical activity from the metallic edge [57]. The activity of semiconducting 2H-MoS₂ phase nanosheets is mainly limited by their high resistance, which hinders charge transfer. The charge transfer kinetics is a key parameter to further improve its performance as a HER catalyst [58]. Based on these reasons, the metallic 1T phase should present excellent catalytic performance, compared to the 2H phase. In 2013, Voiriv et al. directly compared the catalytic performance of MoS₂ in the 2H phase and 1T phase (Figure 3) [59]. In their experiment, the edge of both 1T and 2H were gradually passivated through oxygen. The HER performance decreased with the edge being oxidized in 2H, while it was not degraded during the oxidization in 1T, suggesting that the catalytic effect of 1T mainly derives from the inside of the nanosheet.

The above discoveries promoted research on the catalysis of the 1T phase, and researchers tried many methods to introduce the metallic 1T phase in many other materials. Voiriv et al. synthesized MoS₂ nanosheets with 2H and 1T coexisting on the SiO₂ substrate. Compared to the pure 2H nanosheet, the catalytic efficiency of the 1T and 2H mixed nanosheet was greatly improved [57]. The in-depth analysis suggested that the low contact barrier between the 2H phase and 1T phase led to high electron transfer efficiency in the material in addition to the high activity of the 1T phase. Both factors increased the HER performance. Besides this, the catalytic performance of the 1T phase could be further improved by electron doping. For example, electrons can be injected into MoS₂ to weaken the H atom's adsorption, when single-walled carbon nanotubes (SWCNTs) were deposited on the 1T-MoS₂

monolayer, leading to the acceleration of the HER process [60]. In addition to MoS₂, Chen and Tsai et al. also found excellent HER performance in other TMDs, such as VS₂, NbS₂, and so on [61,62].

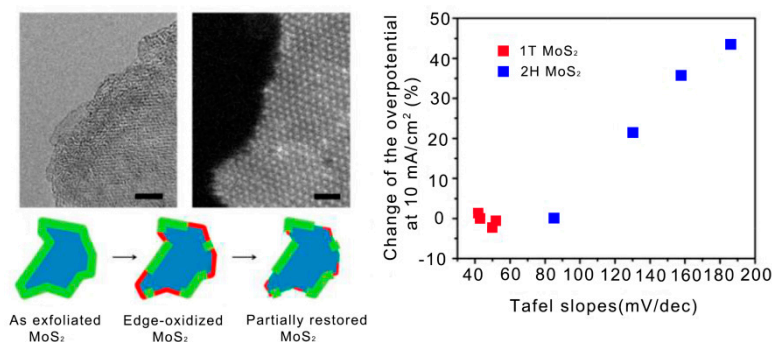


Figure 3. Edge-oxidized MoS₂ nanosheet by TEM and HAADF STEMR and the activity of 1H-MoS₂ and 2H-MoS₂ affected by the oxidation. Reproduced from [59], with the permission of the American Chemical Society.

3.2. Energy Storage

The lithium-ion battery (LIB) is a typical secondary battery with high energy density, long life, large charge and discharge capacity, and low self-discharge, and has, thus, attracted extensive attention. To meet the growing need for applications, such as portable electronic products, electric vehicles, aerospace and other fields, the development of high-performance battery materials is an important subject of current research. Anode materials are very important for the performance of LIBs. Ideal anode materials should possess large capacity, high conductivity, high ion mobility, low cost, chemical stability, and environmental friendliness [63]. TMDs are a kind of potential anode material due to their rapid lithium-ion diffusion interface and more inert surface than those of other materials. A recent study revealed that the typical TMD VS₂ shows excellent cycling performance and capacity when used as anode material of LIBs [64]. The capacity of the VS₂ nanosheet could reach 532.2 mA g⁻¹ after 30 cycles at 50 mA g⁻¹ charge–discharge current. After 100 cycles, the stable discharge capacity was 436.8 and 270.4 mAh g⁻¹ at 100 and 500 mA g⁻¹, respectively. The excellent rate performance and cyclic stability of the material are attributed to higher electronic conductivity and its layered structure. Based on TMDs, there also exist other methods to further improve the performance of LIBs. Zhou et al. composited MoS₂ and graphene to increase the specific surface area, and the stability and capacity of the MoS₂/graphene were greatly increased (1060 mAh g⁻¹) as the anode of LIBs [65]. In addition, the conductivity of 2H-MoS₂ as an anode in LIBs could be improved by introducing the 1T' phase [66]. The resulting capacity was nearly twice that of the pure 2H phase. The capacity could still maintain 636 mAh g⁻¹ at charge and discharge current of 1A g⁻¹ even after 2000 cycles.

Instead of LIBs, TMDs could also serve as the electrodes of supercapacitors due to their high electrical conductivity, small size, and large specific surface area. The supercapacitor shows a much higher capacity than the normal capacitor. More importantly, the lower voltage limitation fills the gap between electrolytic capacitor and rechargeable battery. Supercapacitors are applied in many electronics devices, including regenerative braking, short-term energy storage or burst mode power transfer, and as power backups for static random-access memory (SRAM), which requires fast charging–discharging cycling [67]. In 2007, Soon et al. applied MoS₂ film grown by CVD to the electrode of a supercapacitor. The experimental results showed that the specific surface area of the electrodes increased as the number of layers decreased, resulting in a substantially increased AC frequency and charge accumulation [68]. With the discovery of the 1T phase, Acerce et al. successfully used 1T-MoS₂ as the electrode material for supercapacitors [69]. Compared with previous studies, the volumetric capacitance of 1T-MoS₂ ranged from 400 to 700 Fcm⁻³. Its chem-

ical stability was also improved, and the Coulomb Efficiency remained above 95% after 5000 cycles. VS_2 also presented excellent performance when it was used as the electrode of supercapacitors. Its specific capacitance was up to $4760 \mu\text{F}/\text{cm}^2$ (Figure 4) [70].

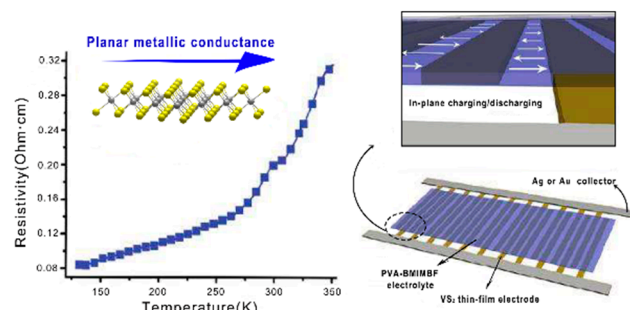


Figure 4. VS_2 as a new type of high performance in-plane supercapacitor based on quasi 2D materials. Reproduced from [70], with the permission of the American Chemical Society.

3.3. Ferroelasticity, Ferroelectricity, and Ferromagnetism

Ferroelasticity, ferroelectricity, and ferromagnetism all describe a hysteresis phenomenon in material under external action induced by a state of low symmetry. The difference is that ferroelasticity is the hysteresis of stress under strain, ferroelectricity is the hysteresis of polarization under an external electric field, and ferromagnetism is the hysteresis of magnetization under an external magnetic field. Multiferroic material is the coupling among the above three ferroics, and, thus, it shows great potential in sensors, transducers, and other devices. The discovery of the above properties in 2D materials has promoted the miniaturization of many devices.

3.3.1. Ferroelasticity

Ferroelasticity is a phenomenon in which a material exhibits spontaneous strain. When stress is applied to a ferroelastic material, it transits among its different stable variants. TMDs show a variety of phase structures, including 2H, 1T, and distorted 1T' phases. Both the 2H phase and the 1T phase are high symmetry structures. However, due to the existence of lattice distortion in the 1T' phase, the symmetry of the crystal structure is reduced leading to ferroelasticity. In 2016, Li et al. reported the mechanical strain-induced orientation transition of the 1T' phase and the thermodynamic stability through first-principles calculation [71]. Figure 5c depicts the three different variants of the 1T' phase in TMDs, which can be regarded as different ferroelastic domains. The strain can be used to regulate variants, and the transition barrier among them could also provide the possibility to trigger phase or variant transition in experiments. For example, the domain transition barrier was about 0.23 eV/f.u. in WTe_2 , while it was 0.21 eV/f.u. in MoS_2 . These results indicated that the ferroelastic domain transition could be achieved under conventional experimental conditions. Regrettably, there is no experimental verification yet, because the calculation results are obtained at 0 K. In addition, the shape memory effect and superelasticity in ferroelasticity also need to be further studied.

3.3.2. Ferroelectricity

Ferroelectricity refers to spontaneous polarization and polarization switching under an external electric field. Ferroelectric polarization switching is often accompanied by the lattice constant changing. Therefore, ferroelectric materials can be used to fabricate electric field-controlled smart driving materials. On the contrary, the electrical polarization could also be changed through strain, and this property is the so-called piezoelectricity. Piezoelectric materials, such as MoS_2 , WS_2 , and WTe_2 show potential in energy conversion devices and sensors.

Duerloo et al. studied ferroelectricity in a series of TMDs through first-principal calculations, in which semiconductive 2H MoS_2 , MoSe_2 , MoT_2 , WS_2 , WSe_2 , and WTe_2 were

proved to be ferroelectric, while metallic 2H NbSe₂ and TaSe₂ were not ferroelectric [72]. Uniaxial strain was also applied on MoS₂ and WS₂ to investigate piezoelectricity, as shown in Figure 5b. The polarization of MoS₂ and WS₂ along the *x*-direction varied linearly with strain and was stronger compared with other 2D materials, such as BN. In addition to the natural ferroelectricity of 2H TMDs, ferroelectricity was also observed in some organic functional group absorbed TMDs, such as -CH₃, CH₂OCH₃, CH₂F, and so on. The electrical polar orientation of these functional groups could be changed under an external electric field. The above ferroelectric materials present great potential for multifunctional electronic devices, such as ferroelectric field-effect transistors with ultra-high on-off ratios, Dirac fermion topology transistors for electron/hole conversion, ultra-high resistance ferroelectric heterojunctions, and multiferroic spin valves controlled by electric fields [73].

In addition to the 2H phase, the 1T' phase is also a potential ferroelectric material due to its low symmetry crystal structure. In 2019, Pankaj et al. discovered ferroelectricity in 1T' phase WTe₂, and the piezoelectric response of this material could reach the nanoscale [74]. As shown in Figure 5a, the ferroelectric domain structure and domain wall of WTe₂ can be clearly observed. Meanwhile, the hysteresis loop and the transition process of the ferroelectric domain could be observed simultaneously by the applied electric field. The saturated iron electrodes could be up to ~0.19 μC/cm². Since the above tests were all tested at room temperature, the results proved that WTe₂ had ferroelectricity at room temperature, which was helpful for its practical application. In addition, the theoretical calculations indicated that the potential barrier was about 0.29 eV/f.u. during the transition of the ferroelectric domain. In the typical ferroelectric material BaTiO₃, the ferroelectric domain transition barrier was about 0.43 eV/f.u. Obviously, ferroelectric domain transition in 1T'-WTe₂ was much easier under the external electric field, suggesting a faster external field response.

The ferroelectricity of all the above-mentioned TMDs originates from the *in-plane* spontaneous polarization. Besides *in-plane* polarization, Qing Yang et al. proposed the *out-of-plane* spontaneous polarization in double-layer 1T-WTe₂ through calculations [75]. Meanwhile, the reversal of the ferroelectric polarization direction can be realized by interlayer sliding. Since the metal ion W is positively charged and the non-metal ion Te is negatively charged, adjusting the stacking of the bilayer WTe₂ by interlayer slip could generate vertical upward or downward electrical polarization. Calculations showed that the sliding barrier of the bilayer structure in the mutually perpendicular electric polarization states (State I and II) was 0.6 MeV.

3.3.3. Ferromagnetism

With the rise of spintronics, spin, another intrinsic property, is treated as the carrier, instead of the electron, expanding the degree of freedom and performance of electronic devices. The unique properties of TMDs meet the relevant performance requirements and have become a novel candidate for spintronic devices. The spin injection is very important for spintronics. The direct method of injection spin to nonmagnetic TMDs is doping magnetic atoms leading to the so-called dilute semiconductor. Ashwin et al. studied the magnetic and electronic structure of Mn-doped 2H-MoS₂ by first-principles and Monte Carlo calculations [76]. When the content of Mn reached ~12.5%, strong ferromagnetic coupling among Mn atoms could be observed, which derived from the double exchange interaction between Mn and the neighboring S. The MoS₂ was still semiconducting after Mn doping. In addition to Mn, it was found that Ti, V, Cr, Fe, Co, Ni, Cu, and Zn doping could also introduce magnetism into MoS₂ [77].

Magnetism can also be induced from the adsorbing atoms on the surface of TMDs such as H, B, C, N, O, and F. At the same time, theoretical calculations show that the adsorption of O and F on MoS₂ has a large spatial spin density and a long-range antiferromagnetic coupling. For H and N atom adsorption, n-type and p-type doped magnetic semiconductors can be achieved [78,79], respectively. However, the Curie temperature of magnetic semiconductors (diluted magnetic semiconductors) obtained by this kind of micro-doping

is too low (only ~ 5 K Curie temperature was observed in Mn-doped MoS_2), which greatly limits the application of this material in spintronics devices [76].

To overcome the disadvantages of dilute magnetic semiconductors, Liang Cai et al. proposed inducing the second phase in non-magnetic semiconductors (Figure 5d) [80]. In their experiments, MoS_2 contained both 2H and 1T phases and a certain amount of S vacancies. The exchange between Mo and S was strengthened and then led to 395 K Curie temperature. In addition, recent studies on natural magnetic transition metals V, Cr, and Mn TMDs also showed a high Curie temperature. The Curie temperature could even reach ~ 1000 K in strained 1T CrSe_2 and 1T CrTe_2 [81]. During the straining process, the transition from antiferromagnetic to ferromagnetic could also be realized.

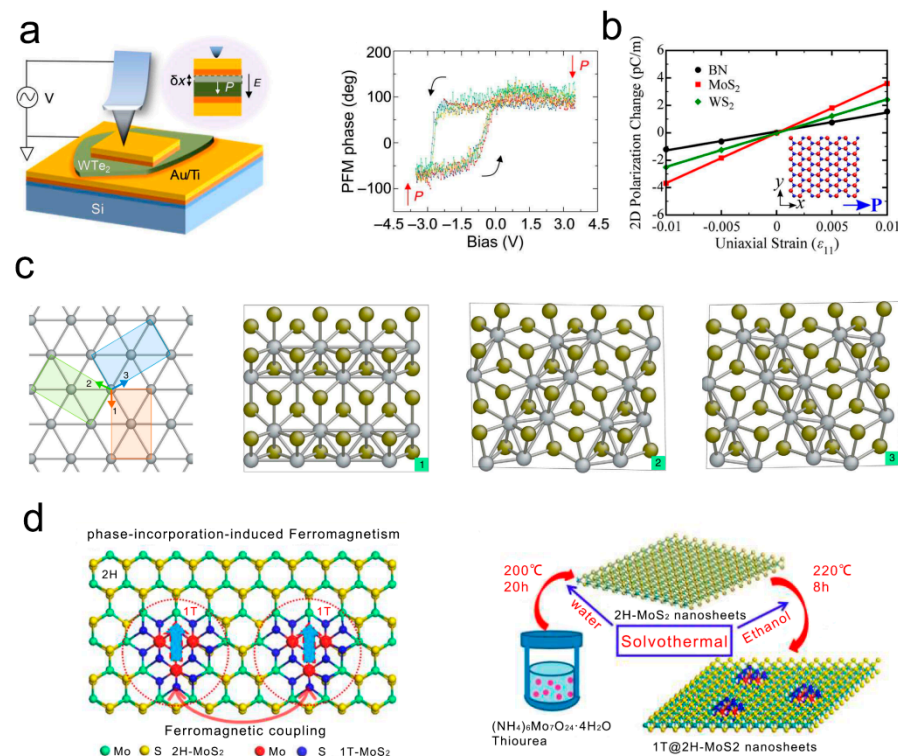


Figure 5. Ferromagnetism, ferroelasticity, and ferroelectricity of TMDs phase structure and their applications. (a) 1T'- WTe_2 displays ferroelectricity at room temperature. Reproduced from [74], with the permission of the AAAS. (b) Polarization of 2D BN, MoS_2 , and WS_2 along the x -direction varies linearly with strain. TMDs have stronger piezoelectricity than BN. Reproduced from [72], with the permission of the American Chemical Society. (c) Tuning strain enables switching between different ferroelastic domains. Reproduced from [71], with the permission of the AAAS. (d) Structure and hydrothermal synthesis of 1T- MoS_2 doped with 2H- MoS_2 . Reproduced from [80], with the permission of the American Chemical Society.

3.4. Electronics Applications

3.4.1. Field Effect Transistor

The field effect transistor (FET) is an electronic device that controls the current through an electric field. The carrier conductivity can be adjusted through the shape of the conduction band under an electric field. FET is widely used in digital integrated circuits, information storage, and other logical operation devices. During the past decades, graphene has attracted considerable attention as the main material of FETs due to its abundant physical properties and high mobility [8]. The special electronic properties and moderate mobility of TMDs provide the possibility to construct excellent FETs. In theoretical calculation, the mobility of single-layer MoS_2 reached $200 \text{ cm}^2 \text{ V}^{-1} \text{ s}^{-1}$, the mobility of ZrS_2 reached $1237 \text{ cm}^2 \text{ V}^{-1} \text{ s}^{-1}$, and the mobility of ZrSe_2 reached $2316 \text{ cm}^2 \text{ V}^{-1} \text{ s}^{-1}$ [82,83]. Yonatan Vaknin fabricated FET based on MoS_2 as shown in Figure 6a [84]. It was also found

that the barrier height at the gold/molybdenum disulfide (MoS_2) interface decreased with the increase of drain voltage, reaching a reduction of 0.5–1 V. An increase in the grid voltage resulted in a decrease in the additional barrier. Radisavljevic fabricated a MoS_2 FET on HfO_2 [83]. The mobility could reach $200 \text{ cm}^2 \text{ V}^{-1} \text{ s}^{-1}$ at room temperature. In addition, the current on/off ratio could reach 108 at room temperature, with ultra-low standby power consumption. In subsequent further studies, the team revealed a temperature-dependent dependence of electron mobility, suggesting that the top dielectric had an inhibitory effect on charge impurity scattering. At the same time, the gate voltage applied to MoS_2 induced metal–insulator transition, which enhanced the interaction between electrons [85]. In a FET, the materials used for the gate, drain, and source are semi-conductive and metallic, respectively, and, therefore, the metal–semiconductor contact interface of different materials leads to a higher Schottky barrier [85], and higher contact resistance ($0.7 \text{ k}\Omega \mu\text{m}$ – $10 \text{ k}\Omega \mu\text{m}$). To solve this problem, Zhang and his teammates grew $2\text{H}/1\text{T}'$ - MoTe_2 lateral heterojunctions through CVD and constructed them as FETs, in which $1\text{T}'$ and 2H phases were used as source and drain, respectively. The Schottky barrier between $1\text{T}'$ and 2H was only $\sim 0.25 \text{ eV}$ [86]. This method was then applied to construct a $2\text{H}/1\text{T}'$ heterojunction FET in MoS_2 . The contact resistance of the device was only 200 – $300 \Omega \mu\text{m}$. In addition, IV B TMDs also showed great potential in FET applications. For example, the on/off ratio of FET composed of ZrS_2 -/ hBN could reach 10^6 . The theoretical mobility of HfSe_2 was up to $3500 \text{ cm}^2 \text{ V}^{-1} \text{ s}^{-1}$, while its on/off ratio was 7.5×10^6 [38].

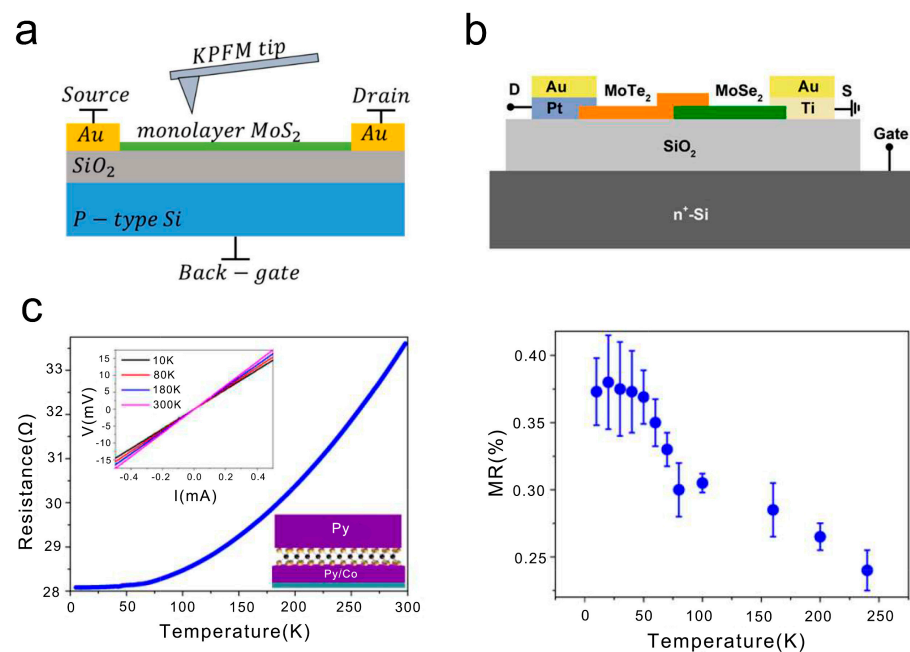


Figure 6. Application of TMDs phase structure electronics. (a) MoS_2 -based FET, schematics of a field-effect transistor (FET) composed of a monolayer molybdenum disulfide (MoS_2) layer as the channel, drain, and source gold terminals, and a back-gate, in addition to the Kelvin probe force microscopy (KPFM) tip. Reproduced from [84], with the permission of the MDPI. (b) Schematic of the $\text{MoTe}_2/\text{MoSe}_2$ heterojunction device. During electrical measurements, the source terminal (S) is grounded while the bias is applied to the drain terminal (D) or Si gate. Reproduced from [87], with the permission of the MDPI. (c) Temperature dependence of junction resistance and magnetoresistance (MR) curves at different temperatures of $\text{NiFe}/\text{MoS}_2/\text{NiFe}/\text{Co}$. Reproduced from [88], with the permission of the American Chemical Society.

3.4.2. Photodetector

A photodetector is used to detect light or other electromagnetic radiation. The core component of the photodetector is the p-n junction, which can convert photons into current or electron-hole pairs in the depletion zone. The photodetector has a wide range of appli-

cations, including light-emitting diode, ion detector, photomultiplier tube, photovoltaic power generation unit, displays, etc. In the application of this device, the essential mechanism is the transition of electrons excited by light radiation. Therefore, the electronic structure is very important to the performance of this device, which mainly affects the absorption and radiation of light. In semiconductors with a direct band gap, the bottom of the conduction band and the top of the valence band are in the same position in the reciprocal space. The electron transition is only related to the band gap and the light frequency, thus leading to very high photoelectric efficiency. In the indirect band-gap semiconductor, the bottom and top of the conduction band are located at different positions in the reciprocal space. In addition to the value of band gap and the frequency of light, the electrons need to shift spatially during the electron transition process, which results in lower absorption excitation efficiency in the semiconductors. As the number of layers decreases, many TMDs transit from indirect band gap semiconductors to direct band-gap semiconductors, such as MoS₂, making TMDs one of the potential candidates for use in photodetectors [89]. In addition, TMDs have a very high response rate, quantum efficiency, and rapid light response as photodetector devices.

At present, many achievements have been made in the study of photoelectric detectors for TMDs. Monolayer and multilayer 2H-MoS₂ have semiconductor properties, and their band gaps are 1.8 eV and 1.6 eV, respectively. They can be effectively detected at exactly the frequency range of green light. When 2H-MoS₂ grows to three layers, the 1.3 eV band gap is suitable for red light detection. In addition to common TMDs, such as MoS₂ and WS₂, other TMDs belonging to the IV B family also show excellent performance in optical and electronic applications. In 2015, He et al. fabricated ultra-sensitive phototransistors using HfS₂ as the main material, with photoelectric response efficiency exceeding 890 AW⁻¹ at a gate voltage of 80 V [90]. In addition to their excellent photoelectric properties, TMDs can be further controlled by changing external conditions, such as stress and electric field, due to the obvious change of band structure under external conditions. For example, in a multilayer WS₂/graphene van der Waals heterostructure, Francesco regulated the photoluminescence in WS₂ through a polymer micro actuator [91]. Then, Fatemeh prepared a MoSe₂/WSe₂ heterojunction used as a solar cell [92]. The electron-hole interaction in this device was very strong. The performance of the device could be improved to 350% in the near-infrared frequency range. Luo prepared a high-response photovoltaic photodetector based on the MoTe₂/MoSe₂ II heterojunction (Figure 6b) [87]. This self-powered photoelectric detector showed a response of 1.5 AW⁻¹. Due to the efficient separation of the electron-hole pair and the ultra-fast charge transfer, the light-induced on-off ratio of the current switch was greater than 10⁴ at zero bias. In addition to the above photoelectric devices, another important application of photodetectors is solar cells. Researchers found that the light conversion efficiency of the solar cell composed of three layers of graphene/MoS₂/n-Si could reach 11.1% [93].

3.4.3. Giant Magnetoresistance and Spin Valve

Spin, another intrinsic property of electrons, was ignored in electronic devices. After the giant magnetoresistance (GMR) effect was first discovered in 1988, utilizing spin began to attract much more attention in electronic devices, which was named as Spintronics. Spintronics extends the degree of freedom of carriers to the intrinsic property of spin. Electronic devices with both electron spin and charge as carriers have shown great potential in modern information technology applications. With the development of 2D materials, breaking the degeneration of electron spin orbits, electrons exhibit new degrees of freedom (valley degrees of freedom) in different spins, providing new possibilities for the development of smaller electronic devices [94]. The simplest spin valve device based on the GMR effect has a three-layer structure, in which two ferromagnetic layers (common materials are magnetic metals, such as Fe, Co, and Ni) are arranged on both sides separated by a non-magnetic layer. One of the two ferromagnetic layers is fixed through the pinning effect from the antiferromagnetic layer, so that the magnetization orientation cannot be changed

by the external magnetic field. The other layer is the free layer, the magnetization orientation of which can be changed by the external magnetic field. When the magnetization orientations of the two ferromagnetic layers are parallel to each other, the spin-up electrons have the lowest resistance, while the spin-polarized electrons, with different magnetization orientations, show higher resistance. When the magnetized orientation of the ferromagnet is antiparallel, the electrons, regardless of spin polarization, are in a high resistance state and are not conductive.

The tunneling magnetoresistance (TMR) effect is similar to GMR, except that the intermediate layer material is made of a non-magnetic insulative or semiconductive material [95]. In TMR, electrons are tunneled from one ferromagnetic layer to another through the tunneling effect. When the magnetization orientations of the two ferromagnets are parallel, the resistances of the polarized electrons are low and the chances of tunneling are high, which characterizes the conduction state. When the magnetization orientation of the two ferromagnets is inversely parallel, the polarized electrons have higher resistance and lower chances of tunneling, characterizing the non-conductive state. The spin valve structure of the TMR is also known as the magnetic tunnel junction (MTJ). Since the tunneling current density is generally small, the magnetoresistance of MTJ devices is usually higher than that of GMR spin valves.

It was observed that a higher magnetoresistance could be obtained by composing TMDs with other materials to form a multi-layer spin valve structure. For example, NiFe/MoS₂/NiFe/Co spin valves have a magnetoresistance of 0.4% at room temperature (Figure 6c) [88]. On this basis, researchers further increased their magnetoresistance to ~0.73% by adding an extra Au layer between the MoS₂ and NiFe layers to avoid oxidation of the NiFe layer. However, the high Schottky limits the spin polarization current and the effective injection of spin. Jen-Ru Chen et al. effectively reduced the Schottky barrier and increased the spin injection efficiency by adding an extra MgO layer between the ferromagnetic electrodes as a transition layer in MoS₂ [96]. In addition, researchers are attempting to reduce Schottky barriers using heterostructures composed of different phases of TMDs as the means of chemical synthesis are improved.

3.5. Thermal Conductivity

Like graphene, TMD material has high mobility of charge carriers at room temperature. However, the thermal conductivity of TMDs is much lower than that of graphene. The thermal conductivity of monolayer TMD material graphene is 2-3 orders of magnitude lower. Cai et al. calculated the room temperature thermal conductivity of MoS₂ as 23.2 MW·m⁻² k⁻¹ by the nonequilibrium Green's function calculation [97]. Monolayer TMD materials are limited by their ultrathin thickness and highly localized Joule heating, resulting in hot spots [98]. This is extremely beneficial for the use of TMDs as thermoelectric materials. Meantime, this greatly affects the performance and reliability of electronic devices based on TMDs. In addition, phonon scattering at the interface plays a key role in heat transfer at the interface [99]. TMD material sheets and other material surface contacts can be divided into two types: side contact and edge contact [100]. In side contact, the metal surface interacts with the basal surface of MoS₂ through van der Waals. At the same time, MoS₂ and graphene have different phonon dispersions (Figure 7) [101], which results in additional electron scattering at the interface, so the interface thermal conductivity is usually lower at the side contact interface. The interfacial thermal conductivity of MoS₂/ graphene is 13.8 MW·m⁻² k⁻¹ [102]. In the edge contact, the interface between monolayer MoS₂ and other materials forms chemical bonds, resulting in high heat transport. The interfacial thermal conductivity of MoS₂/ graphene is 6420 MW·m⁻²·k⁻¹ [103]. When TMDs are used as optoelectronic devices, cooling strategies are needed, which can effectively conduct heat through edge contact with other materials.

The thermal conductivity of TMDs is not only affected by material intrinsic properties and interfaces. It is also related to size, temperature and mechanical strain. Zhang et al. calculated the 1H and 1T'-MoS₂ two-phase thermal conductivities of monolayers by first

principles [104]. The thermal conductivity of 1H and 1T'-MoS₂ monolayer increased with the length of the material and decreased with increase in temperature. Under the influence of mechanical strain, 1H-MoS₂ was almost unaffected, while 1T'-MoS₂ decreased with increase in tensile strain.

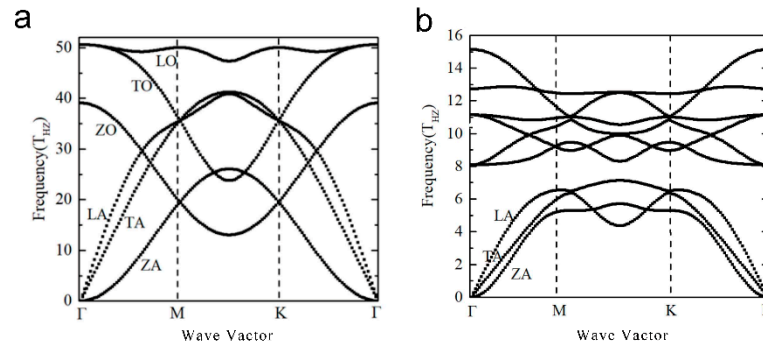


Figure 7. (a) Phonon spectra of monolayer graphene, (b) monolayer MoS₂. Reproduced from [101], with the permission of the MDPI.

4. TMDs' Phase Transition

The abundant phase structures in TMDs, and their corresponding different physical and chemical properties, suggest that phase transitions in 2D TMDs should be more attractive because of the possibility for flexible, low-power, and transfer-efficient electronics. In addition, efficient bulk regulation of phase transitions can also be applied in various fields, such as hydrogen evolution reaction and catalysis. At present, there are two main methods to realize the phase transition in TMDs: strain and electron modulation.

4.1. Strain-Induced Phase Transition

Strain-induced phase transition is one of the most common control methods. The Gibbs free energy (G) is adopted to determine the lowest energy path of the strain-induced phase transition process. According to basic phase transition theory, the Gibbs free energy G of a material can be expressed as:

$$G(P, T) = E_{\text{coh}} + PV - TS \quad (1)$$

where E_{coh} is the cohesive energy of the material (the energy released by the combination of isolated atoms into the material); V is the volume; S is the entropy.

To compare the stability of two different structures, it is necessary to compare the Gibbs free energy changes of the two structures:

$$\Delta G(P, T) = \Delta E_{\text{coh}} + P\Delta V - T\Delta S \quad (2)$$

The value of the first two items of Equation (2) is much larger than the entropy change, so the Gibbs free energy can be simplified as:

$$\Delta G(P, T) \cong \Delta E + P\Delta V \quad (3)$$

All terms in Equation (3) can be easily obtained. The change of the cohesive energy is the difference in the total energy of the two different structures, and the pressure P is the first derivative of the energy to the volume change:

$$P = -\frac{\partial E_{\text{coh}}}{\partial V} \quad (4)$$

It is worth noting that the pressure P in the MoS₂ to be calculated is the applied stress value. The two structures are considered to undergo phase transition when the Gibbs free energies are equal. Therefore, the lowest energy path for the phase transition is the

common tangent of the Gibbs free energies of the two structures. As shown in Figure 8, V_1/V_0 represents the change of the current volume relative to the original volume.

Since the lattice constants of the 2H phase and the 1T or 1T' phase are different, the phase transition of the 2H phase to the 1T or 1T' phase can be achieved by applying a certain degree of strain to the 2H phase in the ground state. Chen et al. provide a feasible solution for low energy consumption small spin electronic devices by adjusting strain to convert 1T'-CrS₂ into spin-up or spin-down semimetals [105]. Reed et al. systematically studied the phase transition process between 2H-1T' of Mo and W chalcogenides under uniaxial and biaxial strains through theoretical calculation [106]. It can be proved that strain is an effective method to adjust the relative energy of two phases. In addition to WTe₂, the 2H phase can be transitioned into 1T' through uniaxial or biaxial stretching. When free energy is close to zero, its phase transition range is $\varepsilon_y = 0.5\%$ to 2.4% (this range is the coexistence of 2H and 1T'). When the strain is greater than 2.4% , the 2H phase completely transits to the 1T' phase. At room temperature, the phase transition range is $\varepsilon_y = 0.3\%$ to 3% . Subsequently, Song et al. experimentally fabricated monolayer MoTe₂ and applied tensile strain to it. Their experimental results demonstrated that the 2H phase gradually undergoes a phase transition from 2H to 1T' when the strain reaches 0.2% at room temperature, which is accompanied by a transition from semiconducting to metallic (Figure 9a) [107].

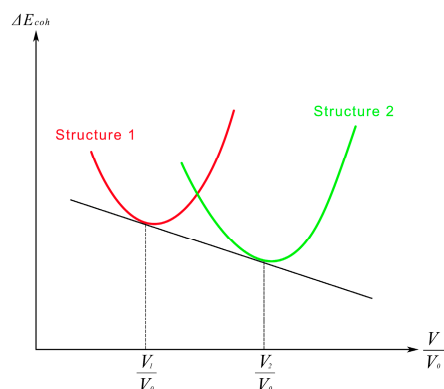


Figure 8. Principle of stress induced transition between two different phases.

4.2. Electron-Controlled Phase Transition

In addition to directly changing the lattice constants of 2H phase and 1T/1T' phase to induce phase transition, controlling the number of electrons in the 2D TMD system can also achieve phase transition due to the different electronic structures and atomic bonds of 2H and 1T/1T' [108,109]. Depending on the specific electronic means of control, phase transition can be achieved by plasma thermoelectrons, beam radiation, electrostatic electron injection, alloying doping, and alkali metal atom adsorption.

4.2.1. Plasma Thermoelectron Induced 2H-1T Phase Transition

In 2014, Yimin Kang proposed a method to induce 2H-1T in MoS₂ by plasma thermoelectrons [96]. Au nanoparticles were deposited on a single 2H-MoS₂ nanosheet. Since the work function of Au atoms is about 5.1 eV, the electrons on the nanoparticles escape and transfer to the MoS₂ nanosheet when an incident laser with a wavelength of 488 nm is applied to irradiate Au nanoparticles. The Schottky barrier between Au nanoparticles and 2H-MoS₂ is less than 0.8 eV in theoretical calculation. Therefore, it provides the basis for electronic injection. In addition to electrons escaping from Au nanoparticles, Au nanoparticles are located above the top S atom. The interaction between Au and MoS₂ weakens the top Mo-S bond, making the top S atom more slippery and the 2H phase unstable [110]. The 2H-MoS₂ is formed because the 4d orbital of the Mo atom splits into three groups through the crystal field of the six nearest S atoms, and its lowest energy level is dz², which results in the 2H phase being the most stable at room temperature. At this time, the symmetry centered on the Mo atom is D_{3h}. The 4d orbits of the Mo atom in the 1T phase are split

into two groups, one of which is the triple degenerate t_{2g} orbitals occupied by two electrons at the lowest energy level. The second is the double degenerate e_g orbitals. Considering that the dz^2 orbitals are already fully occupied, the electrons can only be distributed above higher energy levels when the electrons are injected into the 2H phase, while the extra electrons in the 1T phase can occupy the unoccupied t_{2g} orbitals, making the 1T more stable.

4.2.2. Electron Beam Radiation

Although these methods can effectively control the 2H-1T phase transition in MoS₂, they are not suitable for large-area phase transition or fine control due to the low efficiency of Au nanoparticle deposition and the uncontrollable direction of electron escape. Subsequently, by using in-situ scanning transmission electron microscopy (ISTEM), Yung-Chang Lin found that 2H-MoS₂ can gradually transit to 1T after a certain amount of time of beam radiation [111]. After the irradiation of 2H phase, the S atom in the top layer slides to form a stable 1T phase. In addition to phase transition, the advantage of this method is that the phase transition region can be arbitrarily controlled to form coexisting heterojunctions of 2H and 1T phases. Metal–semiconductor heterojunctions constructed from different materials are usually difficult to achieve, so it is very important for applications in nano-electronic devices. The patterning of phase structure in a single MoS₂ layer can be easily achieved through beam radiation, so electronic devices can be constructed according to specific requirements.

4.2.3. Electrostatic Doping

Phase transition in TMDs can also be achieved by applying a gate voltage (electrostatic doping). In 2016, Reed et al. proposed a method to realize phase transition in TMDs [112]. Their theoretical calculation showed that a certain voltage applied to MoTe₂ (grown on HfO₂ substrate) would promote electrons or holes being injected into MoTe₂ to achieve a phase change between 2H-1T'. The gate voltage in this process was about 2–4 V. The electron concentration change during phase transition in MoTe₂ was -0.29 e/f.u. (cavity injection) or 0.35 e/f.u. (electron injection). At the same time, the gate voltage induced phase transition could be effectively reduced in the W-doped MoTe₂ (Mo_xW_{1-x}Te₂) (Figure 9c). Subsequently, Wang et al. experimentally demonstrated that electrostatic doping is an effective method to control phase transition in TMDs. To achieve electrostatic doping to regulate phase transition, they constructed a FET with a single layer of MoTe₂ as the main component, which was covered with an ionic liquid drop. As the external voltage increased, the electrons in the ionic droplets tended to enter MoTe₂ under the action of an electric field, thus enabling electron injection and phase transition [113]. Reversible phase transition could be achieved by adjusting the gate voltage. This greatly enriches its application prospects in many new applications, such as 2D memory. However, ionic liquid easily reacts with MoTe₂ at room temperature, which greatly limits the phase transition environment of MoTe₂.

4.2.4. Alloying Doping and Alkali Metal Adsorption

Another way to adjust the number of electrons in TMDs is alloying or adsorbing alkali metal atoms on the surface of TMDs. For example, 2H and 1T coexistence could be observed in Mo_{1-x}W_xS₂ [114]. Moreover, both theoretical and experimental studies show that the energies of the 2H and 1T phases gradually approach each other as the W content in MoS₂ or MoTe₂ increases (no more than 0.5). That is, the transition barrier between the two phases gradually decreases. This indicates that the 1T and 2H phase structures easily undergo phase transition after alloying (Figure 9b) [115].

In theoretical calculation, alkali metal elements, such as Li and Na, easily transfer electrons to TMDs when they are adsorbed on the surface of TMDs, thus changing the number of electrons in TMDs. Theoretical calculations show that the Li adsorption increases the stability of the 1T' phase in MoS₂ [116]. When the concentration of Li is beyond 20%, 1T' is more stable than 2H, providing the thermal dynamics conditions for 2H to 1T' transition. At this time, the electron concentration injected into MoS₂ was $8.33 \times 10^{14} \text{ cm}^{-2}$.

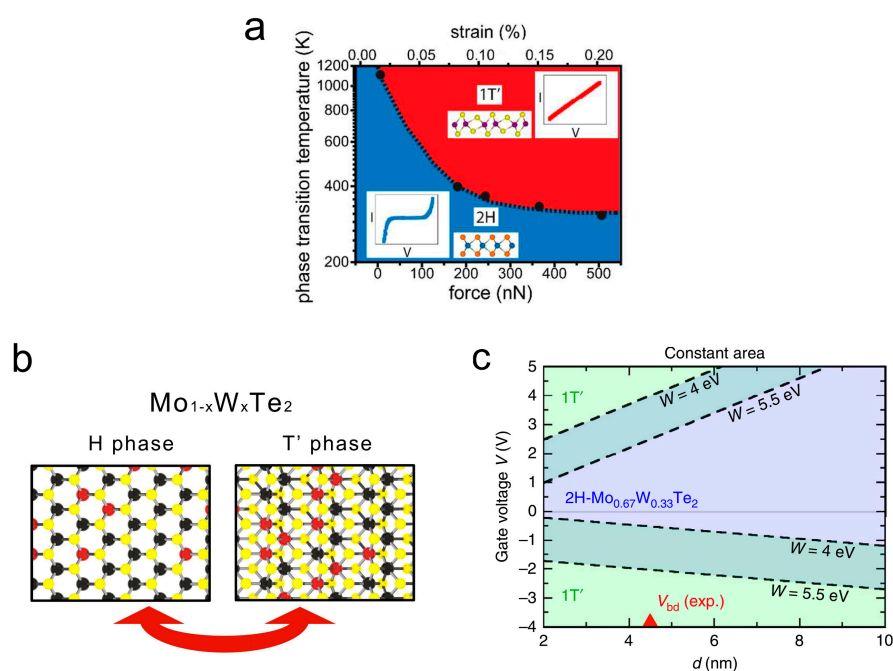


Figure 9. Electron controlled phase transition structure. (a) Temperature–force phase diagram for semiconducting 2H and metallic 1T' MoTe₂. Reproduced from [107], with the permission of the American Chemical Society. (b) Phase structure of WTe₂. Under the doping of Mo atom, WTe₂ changed from the H phase to T' phase. Reproduced from [115], with the permission of the American Chemical Society. (c) Phase boundary at a constant charge in monolayer MoTe₂ and MoS₂. Reproduced from [112], with the permission of the Springer Nature.

5. Summary and Outlook

Since the emergence of TMD, due to its unique physical and chemical properties, it has received extensive attention. This paper reviewed the phase structure of 2D TMD materials, including 2H, 1T, 1T' and CDW. The singular physical and chemical properties of 2D TMDs were also introduced, such as catalytic properties, ferroelasticity, ferroelectricity, ferromagnetism and thermal conductivity properties. Meanwhile, the application of TMDs in electrocatalysis, lithium-ion batteries, supercapacitors, FETs, photodetectors, giant magnetoresistance and spin value are introduced in detail combined with TMDs phase and its characteristics. In addition, we reviewed current methods for modulating TMD phase transitions, including strain-induced and electron-regulated transitions. In particular, we analyzed the advantages and disadvantages of various methods of electron regulated phase transition, including plasma hot electrons, beam radiation, electrostatic electron injection, alloy doping and alkali metal atom adsorption. Further, we looked into the prospect of low symmetry TMDs phase structures for miniaturization applications and edge characteristics of electromechanical devices. Zhu et al. and Chen et al. proposed ultrathin transistors and single-atom layer-thick FinFET devices, respectively [117,118]. The size of electronic components can already reach the thickness of a single layer, and the miniaturized electromechanical devices of this single layer of atoms are also expected to be realized in the future and will have applications in many fields, from bionic robotics to the aerospace industry. However, conventional smart actuation materials exhibit poor performance at the nanoscale, due to detrimental force–length ratio relationships, or performance degradation, due to defective surfaces. Recent studies have shown that 2D smart driver materials are promising candidates for drivers in such devices. These include graphene, graphene oxide, lithium-doped phosphene, and graphite diaynes. However, the limited number of high-performance, 2D smart driving materials severely limits the on-demand design of various applications. The 1T' phase in TMDs has the properties of CDW, that is, coupling between electrons and phonons. At the same time, the 1T phase is very similar

to the 1T' phase and has a large change in the character constant. Therefore, by tuning the CDW state of 1T' or the phase transition between 1T' and 1T, it is expected that smart driving materials with excellent performance could be developed.

It is worth mentioning that MoS₂ in practical applications is not an infinite ideal state, and there are always boundaries. Since the crystal structure and properties of the material at the edge are generally quite different from the internal properties of the material, the material has many novel properties. For example, the 2H phase is used to develop topological insulator materials and properties such as quantum spin Hall effect, edge ferromagnetism [119], and so on. Harnessing the physical properties of the edge is one of the great advantages of 2D materials. Due to the existence of such a low-symmetry phase as that of 1T', its edges may have more diverse edge structures and properties than other phase structures with higher symmetry. So far, there is little research on the edge structure and properties of the 1T' phase. Therefore, through research on the nanoribbons that compose the 1T' phase of MoS₂, it is expected that novel physical and chemical properties will be discovered and will expand the application scope of this type of material.

Author Contributions: H.C., J.Z.: Conceptualization, investigation, writing—original draft. D.K., J.H., M.S., J.P. and S.W.: Investigation. K.C.: Conceptualization, investigation, supervision, writing—review and editing. All authors have read and agreed to the published version of the manuscript.

Funding: This research was funded by National Natural Science Foundation of China (51709150), the National Science Basic Research Plan in the Shaanxi Province of China (2022JQ-012, 2022JQ-521), the Research Startup Fund of the Northwest Institute for Nonferrous Metal Research (YK-2107, YK2114) and Postgraduate Education Innovation Project of Guangdong Ocean University (202256).

Data Availability Statement: Not applicable.

Conflicts of Interest: The authors declare no conflict of interest.

References

1. Novoselov, K.S.; Geim, A.K.; Morozov, S.V.; Jiang, D.; Zhang, Y.; Dubonos, S.V.; Grigorieva, I.V.; Firsov, A.A. Electric field effect in atomically thin carbon films. *Science* **2004**, *306*, 666–669. [[CrossRef](#)]
2. Liu, F.; Ming, P.M.; Li, J. Ab initio calculation of ideal strength and phonon instability of graphene under tension. *Phys. Rev. B* **2007**, *76*, 064120. [[CrossRef](#)]
3. Lee, C.; Wei, X.D.; Kysar, J.W.; Hone, J. Measurement of the elastic properties and intrinsic strength of monolayer graphene. *Science* **2008**, *321*, 385–388. [[CrossRef](#)]
4. Geim, A.K.; Novoselov, K.S. The rise of graphene. *Nat. Mater.* **2007**, *6*, 183–191. [[CrossRef](#)]
5. De Martino, A.; Dell'Anna, L.; Egger, R. Magnetic confinement of massless Dirac fermions in graphene. *Phys. Rev. Lett.* **2007**, *98*, 066802. [[CrossRef](#)]
6. Young, A.F.; Kim, P. Quantum interference and Klein tunnelling in graphene heterojunctions. *Nat. Phys.* **2009**, *5*, 222–226. [[CrossRef](#)]
7. Katsnelson, M.I.; Novoselov, K.S. Graphene: New bridge between condensed matter physics and quantum electrodynamics. *Solid State Commun.* **2007**, *143*, 3–13. [[CrossRef](#)]
8. Castro Neto, A.H.; Guinea, F.; Peres, N.M.R.; Novoselov, K.S.; Geim, A.K. The electronic properties of graphene. *Rev. Mod. Phys.* **2009**, *81*, 109–162. [[CrossRef](#)]
9. Din, H.U.; Idrees, M.; Alam, Q.; Amin, B. Van der Waal heterostructure based on BY (Y = As, P) and MX₂ (M = Mo, W; X = S, Se) monolayers. *Appl. Surf. Sci.* **2021**, *568*, 7. [[CrossRef](#)]
10. Xu, H.W.; Wang, H.; Zhou, J.; Guo, Y.F.; Kong, J.; Li, J. Colossal switchable photocurrents in topological Janus transition metal dichalcogenides. *NPJ Comput. Mater.* **2021**, *7*, 9. [[CrossRef](#)]
11. Zhang, K.; Zhai, J.Y.; Wang, Z.L. A monolayer MoS₂ p-n homogenous photodiode with enhanced photoresponse by piezophototronic effect. *2D Mater.* **2018**, *5*, 8. [[CrossRef](#)]
12. Zhang, C.M.; Nie, Y.H.; Sanvito, S.; Du, A.J. First-Principles Prediction of a Room-Temperature Ferromagnetic Janus VSSe Monolayer with Piezoelectricity, Ferroelasticity, and Large Valley Polarization. *Nano Lett.* **2019**, *19*, 1366–1370. [[CrossRef](#)] [[PubMed](#)]
13. Dastgeer, G.; Afzal, A.M.; Nazir, G.; Sarwar, N. p-GeSe/n-ReS₂ Heterojunction Rectifier Exhibiting A Fast Photoresponse with Ultra-High Frequency-Switching Applications. *Adv. Mater. Interfaces* **2021**, *8*, 9. [[CrossRef](#)]
14. Kwak, D.H.; Jeong, M.H.; Ra, H.S.; Lee, A.Y.; Lee, J.S. Lateral WSe₂ p-n Junction Device Electrically Controlled by a Single-Gate Electrode. *Adv. Opt. Mater.* **2019**, *7*, 8. [[CrossRef](#)]

15. Zibouche, N.; Philipsen, P.; Kuc, A. Strong Variation of Electronic Properties of MoS₂ and WS₂ Nanotubes in the Presence of External Electric Fields. *J. Phys. Chem. C* **2019**, *123*, 3892–3899. [[CrossRef](#)]
16. Woo, Y.; Hong, W.; Yang, S.Y.; Kim, H.J.; Cha, J.H.; Lee, J.E.; Lee, K.J.; Kang, T.; Choi, S.Y. Large-Area CVD-Grown MoS₂ Driver Circuit Array for Flexible Organic Light-Emitting Diode Display. *Adv. Electron. Mater.* **2018**, *4*, 8. [[CrossRef](#)]
17. Yu, S.; Kim, J.S.; Jeon, P.J.; Ahn, J.; Park, J.C.; Im, S. Transition Metal Dichalcogenide-Based Transistor Circuits for Gray Scale Organic Light-Emitting Displays. *Adv. Funct. Mater.* **2017**, *27*, 6. [[CrossRef](#)]
18. Zhang, E.Z.; Wang, W.Y.; Zhang, C.; Jin, Y.B.; Zhu, G.D.; Sun, Q.Q.; Zhang, D.W.; Zhou, P.; Xiu, F.X. Tunable Charge-Trap Memory Based on Few-Layer MoS₂. *ACS Nano* **2015**, *9*, 612–619. [[CrossRef](#)]
19. Han, S.A.; Bhatia, R.; Kim, S.W. Synthesis, properties and potential applications of two-dimensional transition metal dichalcogenides. *Nano. Converg.* **2015**, *2*, 14. [[CrossRef](#)]
20. Chhowalla, M.; Shin, H.S.; Eda, G.; Li, L.J.; Loh, K.P.; Zhang, H. The chemistry of two-dimensional layered transition metal dichalcogenide nanosheets. *Nat. Chem.* **2013**, *5*, 263–275. [[CrossRef](#)]
21. Kim, J.; Lee, E.; Mehta, G.; Choi, W. Stable and high-performance piezoelectric sensor via CVD grown WS₂. *Nanotechnology* **2020**, *31*, 7. [[CrossRef](#)] [[PubMed](#)]
22. Fu, Q.; Han, J.C.; Wang, X.J.; Xu, P.; Yao, T.; Zhong, J.; Zhong, W.W.; Liu, S.W.; Gao, T.L.; Zhang, Z.H.; et al. 2D Transition Metal Dichalcogenides: Design, Modulation, and Challenges in Electrocatalysis. *Adv. Mater.* **2021**, *33*, 24. [[CrossRef](#)]
23. Qian, Z.Y.; Jiao, L.Y.; Xie, L.M. Phase Engineering of Two-Dimensional Transition Metal Dichalcogenides. *Chin. J. Chem.* **2020**, *38*, 753–760. [[CrossRef](#)]
24. Yang, H.; Kim, S.W.; Chhowalla, M.; Lee, Y.H. Structural and quantum-state phase transition in van der Waals layered materials. *Nat. Phys.* **2017**, *13*, 931–937. [[CrossRef](#)]
25. Lu, Q.P.; Yu, Y.F.; Ma, Q.L.; Chen, B.; Zhang, H. 2D Transition-Metal-Dichalcogenide-Nanosheet-Based Composites for Photocatalytic and Electrocatalytic Hydrogen Evolution Reactions. *Adv. Mater.* **2016**, *28*, 1917–1933. [[CrossRef](#)] [[PubMed](#)]
26. Ross, J.S.; Klement, P.; Jones, A.M.; Ghimire, N.J.; Yan, J.Q.; Mandrus, D.G.; Taniguchi, T.; Watanabe, K.; Kitamura, K.; Yao, W.; et al. Electrically tunable excitonic light-emitting diodes based on monolayer WSe₂ p-n junctions. *Nat. Nanotechnol.* **2014**, *9*, 268–272. [[CrossRef](#)]
27. Wang, H.; Yu, L.L.; Lee, Y.H.; Shi, Y.M.; Hsu, A.; Chin, M.L.; Li, L.J.; Dubey, M.; Kong, J.; Palacios, T. Integrated Circuits Based on Bilayer MoS₂ Transistors. *Nano Lett.* **2012**, *12*, 4674–4680. [[CrossRef](#)]
28. Zhang, Z.H.; Zou, X.L.; Crespi, V.H.; Yakobson, B.I. Intrinsic Magnetism of Grain Boundaries in Two-Dimensional Metal Dichalcogenides. *ACS Nano* **2013**, *7*, 10475–10481. [[CrossRef](#)]
29. Liu, L.T.; Kumar, S.B.; Ouyang, Y.; Guo, J. Performance Limits of Monolayer Transition Metal Dichalcogenide Transistors. *IEEE Trans. Electro. Devices* **2011**, *58*, 3042–3047. [[CrossRef](#)]
30. Tang, Q.; Jiang, D.E. Mechanism of Hydrogen Evolution Reaction on 1T-MoS₂ from First Principles. *ACS Catal.* **2016**, *6*, 4953–4961. [[CrossRef](#)]
31. Zhang, Z.X.; Yang, M.Y.; Zhao, N.; Wang, L.; Li, Y.Y. Two-dimensional transition metal dichalcogenides as promising anodes for potassium ion batteries from first-principles prediction. *Phys. Chem. Chem. Phys.* **2019**, *21*, 23441–23446. [[CrossRef](#)] [[PubMed](#)]
32. Bissett, M.A.; Kinloch, I.A.; Dryfe, R.A.W. Characterization of MoS₂-Graphene Composites for High-Performance Coin Cell Supercapacitors. *ACS Appl. Mater. Interfaces* **2015**, *7*, 17388–17398. [[CrossRef](#)] [[PubMed](#)]
33. Xia, J.; Huang, X.; Liu, L.Z.; Wang, M.; Wang, L.; Huang, B.; Zhu, D.D.; Li, J.J.; Gu, C.Z.; Meng, X.M. CVD synthesis of large-area, highly crystalline MoSe₂ atomic layers on diverse substrates and application to photodetectors. *Nanoscale* **2014**, *6*, 8949–8955. [[CrossRef](#)]
34. Du, J.; Xia, C.X.; Xiong, W.Q.; Wang, T.X.; Jia, Y.; Li, J.B. Two-dimensional transition-metal dichalcogenides-based ferromagnetic van der Waals heterostructures. *Nanoscale* **2017**, *9*, 17585–17592. [[CrossRef](#)]
35. Koley, S.; Mohanta, N.; Taraphder, A. Charge density wave and superconductivity in transition metal dichalcogenides. *Eur. Phys. J. B* **2020**, *93*, 8. [[CrossRef](#)]
36. Li, W.B.; Qian, X.F.; Li, J. Phase transitions in 2D materials. *Nat. Rev. Mater.* **2021**, *6*, 829–846. [[CrossRef](#)]
37. Shi, J.P.; Hong, M.; Zhang, Z.P.; Ji, Q.Q.; Zhang, Y.F. Physical properties and potential applications of two-dimensional metallic transition metal dichalcogenides. *Coord. Chem. Rev.* **2018**, *376*, 1–19. [[CrossRef](#)]
38. Yan, C.; Gong, C.; Wangyang, P.; Chu, J.; Hu, K.; Li, C.; Wang, X.; Du, X.; Zhai, T.; Li, Y.; et al. 2D Group IVB Transition Metal Dichalcogenides. *Adv. Funct. Mater.* **2018**, *28*, 1803305. [[CrossRef](#)]
39. Manzeli, S.; Ovchinnikov, D.; Pasquier, D.; Yazyev, O.V.; Kis, A. 2D transition metal dichalcogenides. *Nat. Rev. Mater.* **2017**, *2*, 1–15. [[CrossRef](#)]
40. Liu, X.J.; Zhang, Y.W. Thermal properties of transition-metal dichalcogenide. *Chin. Phys. B* **2018**, *27*, 8. [[CrossRef](#)]
41. Battaglia, C.; Cercellier, H.; Clerc, F.; Despont, L.; Garnier, M.G.; Koitzsch, C.; Aebi, P.; Berger, H.; Forro, L.; Ambrosch-Draxl, C. Fermi-surface-induced lattice distortion in NbTe₂. *Phys. Rev. B* **2005**, *72*, 195114. [[CrossRef](#)]
42. Johannes, M.D.; Mazin, I.I. Fermi surface nesting and the origin of charge density waves in metals. *Phys. Rev. B* **2008**, *77*, 165135. [[CrossRef](#)]
43. Watson, M.D.; Clark, O.J.; Mazzola, F.; Markovic, I.; Sunko, V.; Kim, T.K.; Rosnagel, K.; King, P.D.C. Orbital-and k(z)-Selective Hybridization of Se 4p and Ti 3d States in the Charge Density Wave Phase of TiSe₂. *Phys. Rev. Lett.* **2019**, *122*, 076404. [[CrossRef](#)] [[PubMed](#)]

44. Wen, W.; Zhu, Y.M.; Dang, C.H.; Chen, W.; Xie, L.M. Raman Spectroscopic and Dynamic Electrical Investigation of Multi-State Charge-Wave-Density Phase Transitions in 1T-TaS₂. *Nano Lett.* **2019**, *19*, 1805–1813. [[CrossRef](#)] [[PubMed](#)]
45. Han, T.R.T.; Zhou, F.R.; Malliakas, C.D.; Duxbury, P.M.; Mahanti, S.D.; Kanatzidis, M.G.; Ruan, C.Y. Exploration of metastability and hidden phases in correlated electron crystals visualized by femtosecond optical doping and electron crystallography. *Sci. Adv.* **2015**, *1*, e1400173. [[CrossRef](#)]
46. Fröhlich, H. On the theory of superconductivity: The one-dimensional case. *Proc. R. Soc. London. Ser. A. Math. Phys. Sci.* **1954**, *223*, 296–305.
47. Chan, S.-K.; Heine, V. Spin density wave and soft phonon mode from nesting Fermi surfaces. *J. Phys. F Met. Phys.* **1973**, *3*, 795–809. [[CrossRef](#)]
48. Guillamon, I.; Suderow, H.; Vieira, S.; Cario, L.; Diener, P.; Rodiere, P. Superconducting Density of States and Vortex Cores of 2H-NbS₂. *Phys. Rev. Lett.* **2008**, *101*, 166407. [[CrossRef](#)]
49. Sipos, B.; Kusmartseva, A.F.; Akrap, A.; Berger, H.; Forro, L.; Tutis, E. From Mott state to superconductivity in 1T-TaS(2). *Nat. Mater.* **2008**, *7*, 960–965. [[CrossRef](#)]
50. Stamenkovic, V.R.; Mun, B.S.; Arenz, M.; Mayrhofer, K.J.J.; Lucas, C.A.; Wang, G.F.; Ross, P.N.; Markovic, N.M. Trends in electrocatalysis on extended and nanoscale Pt-bimetallic alloy surfaces. *Nat. Mater.* **2007**, *6*, 241–247. [[CrossRef](#)]
51. Chen, G.X.; Xu, C.F.; Huang, X.Q.; Ye, J.Y.; Gu, L.; Li, G.; Tang, Z.C.; Wu, B.H.; Yang, H.Y.; Zhao, Z.P.; et al. Interfacial electronic effects control the reaction selectivity of platinum catalysts. *Nat. Mater.* **2016**, *15*, 564–569. [[CrossRef](#)] [[PubMed](#)]
52. Feng, Q.C.; Zhao, S.; Wang, Y.; Dong, J.C.; Chen, W.X.; He, D.S.; Wang, D.S.; Yang, J.; Zhu, Y.M.; Zhu, H.L.; et al. Isolated Single-Atom Pd Sites in Intermetallic Nanostructures: High Catalytic Selectivity for Semihydrogenation of Alkynes. *J. Am. Chem. Soc.* **2017**, *139*, 7294–7301. [[CrossRef](#)] [[PubMed](#)]
53. Feng, H.F.; Xu, Z.F.; Zhuang, J.C.; Wang, L.; Liu, Y.N.; Xu, X.; Song, L.; Hao, W.C.; Du, Y. Role of Charge Density Wave in Monatomic Assembly in Transition Metal Dichalcogenides. *Adv. Funct. Mater.* **2019**, *29*, 1900367. [[CrossRef](#)]
54. Zhang, Y.; Yao, Y.Y.; Sendeku, M.G.; Yin, L.; Zhan, X.Y.; Wang, F.; Wang, Z.X.; He, J. Recent Progress in CVD Growth of 2D Transition Metal Dichalcogenides and Related Heterostructures. *Adv. Mater.* **2019**, *31*, 30. [[CrossRef](#)] [[PubMed](#)]
55. Hinnemann, B.; Moses, P.G.; Bonde, J.; Jorgensen, K.P.; Nielsen, J.H.; Horch, S.; Chorkendorff, I.; Norskov, J.K. Biomimetic hydrogen evolution: MoS₂ nanoparticles as catalyst for hydrogen evolution. *J. Am. Chem. Soc.* **2005**, *127*, 5308–5309. [[CrossRef](#)]
56. Jaramillo, T.F.; Jorgensen, K.P.; Bonde, J.; Nielsen, J.H.; Horch, S.; Chorkendorff, I. Identification of active edge sites for electrochemical H₂ evolution from MoS₂ nanocatalysts. *Science* **2007**, *317*, 100–102. [[CrossRef](#)]
57. Voiry, D.; Fullon, R.; Yang, J.E.; Silva, C.; Kappera, R.; Bozkurt, I.; Kaplan, D.; Lagos, M.J.; Batson, P.E.; Gupta, G.; et al. The role of electronic coupling between substrate and 2D MoS₂ nanosheets in electrocatalytic production of hydrogen. *Nat. Mater.* **2016**, *15*, 1003–1009. [[CrossRef](#)]
58. Bollinger, M.V.; Lauritsen, J.V.; Jacobsen, K.W.; Norskov, J.K.; Helveg, S.; Besenbacher, F. One-dimensional metallic edge states in MoS₂. *Phys. Rev. Lett.* **2001**, *87*, 196803. [[CrossRef](#)]
59. Voiry, D.; Salehi, M.; Silva, R.; Fujita, T.; Chen, M.W.; Asefa, T.; Shenoy, V.B.; Eda, G.; Chhowalla, M. Conducting MoS₂ Nanosheets as Catalysts for Hydrogen Evolution Reaction. *Nano Lett.* **2013**, *13*, 6222–6227. [[CrossRef](#)]
60. Liu, Q.; Fang, Q.; Chu, W.S.; Wan, Y.Y.; Li, X.L.; Xu, W.Y.; Habib, M.; Tao, S.; Zhou, Y.; Liu, D.B.; et al. Electron-Doped 1T-MoS₂ via Interface Engineering for Enhanced Electrocatalytic Hydrogen Evolution. *Chem. Mater.* **2017**, *29*, 4738–4744. [[CrossRef](#)]
61. Chen, X.B.; Wang, G.J. Tuning the hydrogen evolution activity of MS₂ (M = Mo or Nb) monolayers by strain engineering. *Phys. Chem. Chem. Phys.* **2016**, *18*, 9388–9395. [[CrossRef](#)] [[PubMed](#)]
62. Tsai, C.; Chan, K.R.; Norskov, J.K.; Abild-Pedersen, F. Theoretical insights into the hydrogen evolution activity of layered transition metal dichalcogenides. *Surf. Sci.* **2015**, *640*, 133–140. [[CrossRef](#)]
63. Dwivedi, S. Solid oxide fuel cell: Materials for anode, cathode and electrolyte. *Int. J. Hydrog. Energy* **2020**, *45*, 23988–24013. [[CrossRef](#)]
64. Cai, L.T.; Zhang, Q.; Mwisizerwa, J.P.; Wan, H.L.; Yang, X.L.; Xu, X.X.; Yao, X.Y. Highly Crystalline Layered VS₂. Nanosheets for All-Solid-State Lithium Batteries with Enhanced Electrochemical Performances. *Acs Appl. Mater. Interfaces* **2018**, *10*, 10053–10063. [[CrossRef](#)] [[PubMed](#)]
65. Zhou, X.F.; Wang, Z.; Chen, W.X.; Ma, L.; Chen, D.Y.; Lee, J.Y. Facile synthesis and electrochemical properties of two dimensional layered MoS₂/graphene composite for reversible lithium storage. *J. Power Sources* **2014**, *251*, 264–268. [[CrossRef](#)]
66. Leng, K.; Chen, Z.X.; Zhao, X.X.; Tang, W.; Tian, B.B.; Nai, C.T.; Zhou, W.; Loh, K.P. Phase Restructuring in Transition Metal Dichalcogenides for Highly Stable Energy Storage. *Acs Nano* **2016**, *10*, 9208–9215. [[CrossRef](#)]
67. Li, Y.; Zhang, J.W.; Chen, Q.G.; Xia, X.H.; Chen, M.H. Emerging of Heterostructure Materials in Energy Storage: A Review. *Adv. Mater.* **2021**, *33*, 2100855. [[CrossRef](#)]
68. Soon, J.M.; Loh, K.P. Electrochemical double-layer capacitance of MoS₂ nanowall films. *Electrochem. Solid State Lett.* **2007**, *10*, A250–A254. [[CrossRef](#)]
69. Acerce, M.; Voiry, D.; Chhowalla, M. Metallic 1T phase MoS₂ nanosheets as supercapacitor electrode materials. *Nat. Nanotechnol.* **2015**, *10*, 313–318. [[CrossRef](#)]
70. Feng, J.; Sun, X.; Wu, C.Z.; Peng, L.L.; Lin, C.W.; Hu, S.L.; Yang, J.L.; Xie, Y. Metallic Few-Layered VS₂ Ultrathin Nanosheets: High Two-Dimensional Conductivity for In-Plane Supercapacitors. *J. Am. Chem. Soc.* **2011**, *133*, 17832–17838. [[CrossRef](#)]

71. Li, W.B.; Li, J. Ferroelasticity and domain physics in two-dimensional transition metal dichalcogenide monolayers. *Nat. Commun.* **2016**, *7*, 10843. [[CrossRef](#)] [[PubMed](#)]
72. Duerloo, K.A.N.; Ong, M.T.; Reed, E.J. Intrinsic Piezoelectricity in Two-Dimensional Materials. *J. Phys. Chem. Lett.* **2012**, *3*, 2871–2876. [[CrossRef](#)]
73. Wu, M.H.; Dong, S.; Yao, K.L.; Liu, J.M.; Zeng, X.C. Ferroelectricity in Covalently functionalized Two-dimensional Materials: Integration of High-mobility Semiconductors and Nonvolatile Memory. *Nano Lett.* **2016**, *16*, 7309–7315. [[CrossRef](#)] [[PubMed](#)]
74. Sharma, P.; Xiang, F.X.; Shao, D.F.; Zhang, D.W.; Tsymbal, E.Y.; Hamilton, A.R.; Seidel, J. A room-temperature ferroelectric semimetal. *Sci. Adv.* **2019**, *5*, eaax5080. [[CrossRef](#)]
75. Yang, Q.; Wu, M.H.; Li, J. Origin of Two-Dimensional Vertical Ferroelectricity in WTe₂ Bilayer and Multilayer. *J. Phys. Chem. Lett.* **2018**, *9*, 7160–7164. [[CrossRef](#)]
76. Ramasubramaniam, A.; Naveh, D. Mn-doped monolayer MoS₂: An atomically thin dilute magnetic semiconductor. *Phys. Rev. B* **2013**, *87*, 195201. [[CrossRef](#)]
77. Yun, W.S.; Lee, J.D. Unexpected strong magnetism of Cu doped single-layer MoS₂ and its origin. *Phys. Chem. Chem. Phys.* **2014**, *16*, 8990–8996. [[CrossRef](#)]
78. Xu, W.B.; Huang, B.J.; Li, P.; Li, F.; Zhang, C.W.; Wang, P.J. The electronic structure and optical properties of Mn and B, C, N co-doped MoS₂ monolayers. *Nanoscale Res. Lett.* **2014**, *9*, 554. [[CrossRef](#)]
79. He, J.G.; Wu, K.C.; Sa, R.J.; Li, Q.H.; Wei, Y.Q. Magnetic properties of nonmetal atoms absorbed MoS₂ monolayers. *Appl. Phys. Lett.* **2010**, *96*, 082504. [[CrossRef](#)]
80. Cai, L.; He, J.F.; Liu, Q.H.; Yao, T.; Chen, L.; Yan, W.S.; Hu, F.C.; Jiang, Y.; Zhao, Y.D.; Hu, T.D.; et al. Vacancy-Induced Ferromagnetism of MoS₂ Nanosheets. *J. Am. Chem. Soc.* **2015**, *137*, 2622–2627. [[CrossRef](#)]
81. Lv, H.Y.; Lu, W.J.; Shao, D.F.; Liu, Y.; Sun, Y.P. Strain-controlled switch between ferromagnetism and antiferromagnetism in 1T-CrX₂ (X = Se, Te) monolayers. *Phys. Rev. B* **2015**, *92*, 214419. [[CrossRef](#)]
82. Zhang, W.X.; Huang, Z.S.; Zhang, W.L.; Li, Y.R. Two-dimensional semiconductors with possible high room temperature mobility. *Nano. Res.* **2014**, *7*, 1731–1737. [[CrossRef](#)]
83. Radisavljevic, B.; Radenovic, A.; Brivio, J.; Giacometti, V.; Kis, A. Single-layer MoS₂ transistors. *Nat. Nanotechnol.* **2011**, *6*, 147–150. [[CrossRef](#)] [[PubMed](#)]
84. Vaknin, Y.; Dagan, R.; Rosenwaks, Y. Schottky Barrier Height and Image Force Lowering in Monolayer MoS₂ Field Effect Transistors. *Nanomaterials* **2020**, *10*, 2346. [[CrossRef](#)]
85. Radisavljevic, B.; Kis, A. Mobility engineering and a metal-insulator transition in monolayer MoS₂. *Nat. Mater.* **2013**, *12*, 815–820. [[CrossRef](#)]
86. Zhang, X.; Jin, Z.; Wang, L.; Hachtel, J.A.; Villarreal, E.; Wang, Z.; Ha, T.; Nakanishi, Y.; Tiwary, C.S.; Lai, J.; et al. Low Contact Barrier in 2H/1T' MoTe₂ In-Plane Heterostructure Synthesized by Chemical Vapor Deposition. *Acs Appl. Mater. Interfaces* **2019**, *11*, 12777–12785. [[CrossRef](#)]
87. Luo, H.; Wang, B.L.; Wang, E.Z.; Wang, X.W.; Sun, Y.F.; Liu, K. High-Responsivity Photovoltaic Photodetectors Based on MoTe₂/MoSe₂ van der Waals Heterojunctions. *Crystals* **2019**, *9*, 315. [[CrossRef](#)]
88. Wang, W.; Narayan, A.; Tang, L.; Dolui, K.; Liu, Y.; Yuan, X.; Jin, Y.; Wu, Y.; Rungger, I.; Sanvito, S.; et al. Spin-Valve Effect in NiFe/MoS₂/NiFe Junctions. *Nano Lett.* **2015**, *15*, 5261–5267. [[CrossRef](#)]
89. Duan, X.D.; Wang, C.; Pan, A.L.; Yu, R.Q.; Duan, X.F. Two-dimensional transition metal dichalcogenides as atomically thin semiconductors: Opportunities and challenges. *Chem. Soc. Rev.* **2015**, *44*, 8859–8876. [[CrossRef](#)]
90. Enoki, T.; Kobayashi, Y.; Fukui, K.I. Electronic structures of graphene edges and nanographene. *Int. Rev. Phys. Chem.* **2007**, *26*, 609–645. [[CrossRef](#)]
91. Colangelo, F.; Morandi, A.; Forti, S.; Fabbri, F.; Coletti, C.; Di Girolamo, F.V.; Di Lieto, A.; Tonelli, M.; Tredicucci, A.; Pitanti, A.; et al. Local tuning of WS₂ photoluminescence using polymeric micro-actuators in a monolithic van der Waals heterostructure. *Appl. Phys. Lett.* **2019**, *115*, 183101. [[CrossRef](#)]
92. Barati, F.; Grossnickle, M.; Su, S.S.; Lake, R.K.; Aji, V.; Gabor, N.M. Hot carrier-enhanced interlayer electron-hole pair multiplication in 2D semiconductor heterostructure photocells. *Nat. Nanotechnol.* **2017**, *12*, 1134–1139. [[CrossRef](#)] [[PubMed](#)]
93. Tsuboi, Y.; Wang, F.J.; Kozawa, D.; Funahashi, K.; Mouri, S.; Miyauchi, Y.; Takenobu, T.; Matsuda, K. Enhanced photovoltaic performances of graphene/Si solar cells by insertion of a MoS₂ thin film. *Nanoscale* **2015**, *7*, 14476–14482. [[CrossRef](#)]
94. Zhao, C.; Norden, T.; Zhang, P.; Zhao, P.; Cheng, Y.; Sun, F.; Parry, J.P.; Taheri, P.; Wang, J.; Yang, Y.; et al. Enhanced valley splitting in monolayer WSe₂ due to magnetic exchange field. *Nat. Nanotechnol.* **2017**, *12*, 757–762. [[CrossRef](#)]
95. Inoue, J.; Maekawa, S. Theory of tunneling magnetoresistance in granular magnetic films. *Phys. Rev. B Condens. Matter* **1996**, *53*, R11927–R11929. [[CrossRef](#)]
96. Kang, Y.M.; Najmaei, S.; Liu, Z.; Bao, Y.J.; Wang, Y.M.; Zhu, X.; Halas, N.J.; Nordlander, P.; Ajayan, P.M.; Lou, J.; et al. Plasmonic Hot Electron Induced Structural Phase Transition in a MoS₂ Monolayer. *Adv. Mater.* **2014**, *26*, 6467–6471. [[CrossRef](#)] [[PubMed](#)]
97. Cai, Y.Q.; Lan, J.H.; Zhang, G.; Zhang, Y.W. Lattice vibrational modes and phonon thermal conductivity of monolayer MoS₂. *Phys. Rev. B* **2014**, *89*, 8. [[CrossRef](#)]
98. Balandin, A.A. Thermal properties of graphene and nanostructured carbon materials. *Nat. Mater.* **2011**, *10*, 569–581. [[CrossRef](#)]
99. Chen, C.C.; Li, Z.; Shi, L.; Cronin, S.B. Thermal interface conductance across a graphene/hexagonal boron nitride heterojunction. *Appl. Phys. Lett.* **2014**, *104*, 4. [[CrossRef](#)]

100. Allain, A.; Kang, J.H.; Banerjee, K.; Kis, A. Electrical contacts to two-dimensional semiconductors. *Nat. Mater.* **2015**, *14*, 1195–1205. [[CrossRef](#)]
101. Wu, S.; Wang, J.F.; Xie, H.Q.; Guo, Z.X. Interfacial Thermal Conductance across Graphene/MoS₂ van der Waals Heterostructures. *Energies* **2020**, *13*, 5851. [[CrossRef](#)]
102. Ding, Z.W.; Pei, Q.X.; Jiang, J.W.; Huang, W.X.; Zhang, Y.W. Interfacial thermal conductance in graphene/MoS₂ heterostructures. *Carbon* **2016**, *96*, 888–896. [[CrossRef](#)]
103. Liu, X.J.; Gao, J.F.; Zhang, G.; Zhang, Y.W. MoS₂-graphene in-plane contact for high interfacial thermal conduction. *Nano Res.* **2017**, *10*, 2944–2953. [[CrossRef](#)]
104. Zhang, C.; Wang, C.X.; Rabczuk, T. Thermal conductivity of single-layer MoS₂: A comparative study between 1H and 1T' phases. *Phys. E* **2018**, *103*, 294–299. [[CrossRef](#)]
105. Chen, K.Y.; Deng, J.K.; Yan, Y.; Shi, Q.; Chang, T.Y.; Ding, X.D.; Sun, J.; Yang, S.; Liu, J.Z. Diverse electronic and magnetic properties of CrS₂ enabling strain-controlled 2D lateral heterostructure spintronic devices. *NPJ Comput. Mater.* **2021**, *7*, 1–9. [[CrossRef](#)]
106. Duerloo, K.A.N.; Li, Y.; Reed, E.J. Structural phase transitions in two-dimensional Mo- and W-dichalcogenide monolayers. *Nat. Commun.* **2014**, *5*, 4214. [[CrossRef](#)]
107. Song, S.; Keum, D.H.; Cho, S.; Perello, D.; Kim, Y.; Lee, Y.H. Room Temperature Semiconductor-Metal Transition of MoTe₂ Thin Films Engineered by Strain. *Nano Lett.* **2016**, *16*, 188–193. [[CrossRef](#)]
108. Chen, K.Y.; Deng, J.K.; Kan, D.X.; Yan, Y.; Shi, Q.; Huo, W.T.; Song, M.S.; Yang, S.; Liu, J.Z. Ferromagnetic and nonmagnetic 1T' charge density wave states in transition metal dichalcogenides: Physical mechanisms and charge doping induced reversible transition. *Phys. Rev. B* **2022**, *105*, 024414. [[CrossRef](#)]
109. Chen, K.Y.; Deng, J.K.; Shi, Q.; Ding, X.D.; Sun, J.; Yang, S.; Liu, J.Z. Charge doping induced reversible multistep structural phase transitions and electromechanical actuation in two-dimensional 1T'-MoS₂. *Nanoscale* **2020**, *12*, 12541–12550. [[CrossRef](#)]
110. Splendiani, A.; Sun, L.; Zhang, Y.B.; Li, T.S.; Kim, J.; Chim, C.Y.; Galli, G.; Wang, F. Emerging Photoluminescence in Monolayer MoS₂. *Nano Lett.* **2010**, *10*, 1271–1275. [[CrossRef](#)]
111. Lin, Y.C.; Dumcenccon, D.O.; Huang, Y.S.; Suenaga, K. Atomic mechanism of the semiconducting-to-metallic phase transition in single-layered MoS₂. *Nat. Nanotechnol.* **2014**, *9*, 391–396. [[CrossRef](#)] [[PubMed](#)]
112. Li, Y.; Duerloo, K.A.N.; Wauson, K.; Reed, E.J. Structural semiconductor-to-semimetal phase transition in two-dimensional materials induced by electrostatic gating. *Nat. Commun.* **2016**, *7*, 1–8. [[CrossRef](#)] [[PubMed](#)]
113. Wang, Y.; Xiao, J.; Zhu, H.Y.; Li, Y.; Alsaied, Y.; Fong, K.Y.; Zhou, Y.; Wang, S.Q.; Shi, W.; Wang, Y.; et al. Structural phase transition in monolayer MoTe₂ driven by electrostatic doping. *Nature* **2017**, *550*, 487–491. [[CrossRef](#)] [[PubMed](#)]
114. Rhodes, D.; Chenet, D.A.; Janicek, B.E.; Nyby, C.; Lin, Y.; Jin, W.; Edelberg, D.; Mannebach, E.; Finney, N.; Antony, A.; et al. Engineering the Structural and Electronic Phases of MoTe₂ through W Substitution. *Nano Lett.* **2017**, *17*, 1616–1622. [[CrossRef](#)]
115. Duerloo, K.A.N.; Reed, E.J. Structural Phase Transitions by Design in Monolayer Alloys. *Acs Nano* **2016**, *10*, 289–297. [[CrossRef](#)]
116. Kan, M.; Wang, J.Y.; Li, X.W.; Zhang, S.H.; Li, Y.W.; Kawazoe, Y.; Sun, Q.; Jena, P. Structures and Phase Transition of a MoS₂ Monolayer. *J. Phys. Chem. C* **2014**, *118*, 1515–1522. [[CrossRef](#)]
117. Zhu, Y.B.; Li, Y.J.; Arefe, G.; Burke, R.A.; Tan, C.; Hao, Y.F.; Liu, X.C.; Liu, X.; Yoo, W.J.; Dubey, M.; et al. Monolayer Molybdenum Disulfide Transistors with Single-Atom-Thick Gates. *Nano Lett.* **2018**, *18*, 3807–3813. [[CrossRef](#)]
118. Chen, M.L.; Sun, X.D.; Liu, H.; Wang, H.W.; Zhu, Q.B.; Wang, S.S.; Du, H.F.; Dong, B.J.; Zhang, J.; Sun, Y.; et al. A FinFET with one atomic layer channel. *Nat. Commun.* **2020**, *11*, 7. [[CrossRef](#)]
119. Chen, K.Y.; Deng, J.K.; Ding, X.D.; Sun, J.; Yang, S.; Liu, J.Z. Ferromagnetism of 1T'-MoS₂ Nanoribbons Stabilized by Edge Reconstruction and Its Periodic Variation on Nanoribbons Width. *J. Am. Chem. Soc.* **2018**, *140*, 16206–16212. [[CrossRef](#)]